STUDIES OF ION TRANSPORT IN GASES; APPLICATIONS IN NUCLEAR PHYSICS

BY
KARI PERÄJÄRVI

Academic Dissertation
for the Degree of
Doctor of Philosophy

Jyväskylä, Finland
March 2001

STUDIES OF ION TRANSPORT IN GASES; APPLICATIONS IN NUCLEAR PHYSICS

BY
KARI PERÄJÄRVI

Academic Dissertation
for the Degree of
Doctor of Philosophy

To be presented, by permission of the
Faculty of Mathematics and Natural Sciences
of the University of Jyväskylä,
for public examination in Auditorium FYS-1 of the
University of Jyväskylä on March 17, 2001
at 12 o'clock noon

Jyväskylä, Finland
March 2001

Preface

The studies reported in this thesis were carried out during the years 1996–2000 at the Department of Physics of the University of Jyväskylä. Now at the end of the project the time has come to express my gratitude to the people who have been heavily involved in it.

First of all, I would like to thank my supervisors, Professor Juha Äystö and Professor Jussi Timonen, for their guidance and support during the years. Without their contribution I would not be in a position to be writing this preface.

I am also very grateful to Professor (Emeritus) Pertti Lipas, who has also been like a supervisor to me.

Experimental nuclear physics is almost always group work. I have had the privilege to be a member of an excellent group throughout these years. I want to thank the former and present IGISOL group members for the times we have shared. Especially I would like to thank Dr Peter Dendooven, Dr Antti Honkanen, Dr Mika Huhta, Mr Jussi Huikari, Dr Ari Jokinen, Mr Arto Nieminen, Dr Markku Oinonen and Dr Teemu Siiskonen for pleasant and productive collaboration.

Finally, I would like to thank my beloved wife, Kirsi, for her endless understanding and support during these years.

Jyväskylä, March 2001

Kari Peräjärvi

Abstract

This thesis is centred around the principle of the Ion Guide Isotope Separator On-Line (IGISOL). First, ion transportation in the IGISOL gas cell is studied. As the main result, a method is developed to simulate the evacuation of ions from the gas cell. Secondly, decay properties of neutron-deficient ^{23}Al and ^{58}Cu nuclei are examined using the IGISOL facility. The decay properties of ^{23}Al are of astrophysical interest, while ^{58}Cu decay is important for studies of Gamow–Teller strength.

Contents

1. Introduction

The Ion Guide Isotope Separator On-Line (IGISOL) technique was developed at the University of Jyväskylä in the early 1980s for the study of exotic nuclei [Ärj81a, Ärj81b]. The IGISOL system derives from the He-jet [Äys77] and On-Line Isotope Separator (ISOL) [Rav94] techniques. The physical working principle of the conventional IGISOL system was widely introduced in Juha Ärje's thesis work in 1986 [Ärj86]. Continuous development work has kept IGISOL as one of the most competitive techniques for studying exotic nuclei [Den97, Äys01]. Interest in the IGISOL has lately been increasing also in other nuclear physics communities. The basic idea behind the IGISOL is so powerful that it has been integrated into several future projects all around the world. As an example, one of these is the Rare Isotope Accelerator (RIA) project in the United States, where a so-called gas-catcher/ion guide will be installed after a fragment separator [RIA00]. The purpose is to use it as part of a chemically unselective ion source for low-energy radioactive ions.

The present thesis work is completely centred around the IGISOL principle. The first part is dedicated mainly to ion guide studies. In that section a more complete picture is given of ion motions in the target chamber buffer gas. This includes the development of a method to compute the macroscopic flow field inside the target chamber. Also a relation between thermal motion and macroscopic flow is explored from the single-ion point of view. Finally, a program is introduced to simulate the motion of thermalized reaction products in realistic target chambers. Throughout these studies one principle was kept in mind: the resulting model should be accurate but at the same time as simple and instructive as possible. At the end of the first section, a comparison is made between computer simulations and sophisticated flow measurements. A discussion is also given of the first results of a project initiated at the IGISOL facility of the University of Jyväskylä to study certain aspects of the gas-catcher/ion guide.

The second part of the thesis concentrates on nuclear spectroscopy. First a short introduction to the field is given, and then the results of two specific experiments at the

Jyväskylä IGISOL facility are presented. In the first experiment, beta decay of ^{23}Al to excited states of ^{23}Mg was studied using low-energy proton and high-energy gamma-ray detection. From the data we identified five gamma transitions belonging to the beta decay of ^{23}Al and six beta-delayed proton transitions from the excited levels of ^{23}Mg to the ground state of ^{22}Na. From the astrophysical point of view the most interesting result was the observation of the decay of the Isobaric Analogue State (IAS), only 222(2) keV above the proton separation energy, in ^{23}Mg by both proton and gamma emission. Extracted proton and gamma decay widths allowed us to calculate the important resonance strength for the IAS. This resonance strength and the more accurately determined energy of the IAS improve the precision of the reaction rate calculation which describes astrophysical nucleosynthesis.

For a charge-exchange reaction such as (p, n), the cross section near zero scattering angle, i.e. $\sigma(0°)$, is expected to be proportional to the Gamow–Teller (GT) transition strength B(GT). Two measurements were recently carried out to test this relationship in ^{58}Cu [Fuj96, Jok98]. In both of these studies the ground-state-to-ground-state GT strength from the ^{58}Cu beta decay experiment of Jongsma et al. [Jon72] was used to provide the normalization factor between $\sigma(0°)$ and the corresponding B(GT) value. Because the work of Jongsma et al. does not include sufficient experimental details, and in view of the importance of this value, the ground-state branching in ^{58}Cu was remeasured at GSI and Jyväskylä. The ^{58}Cu beta decay experiment performed at Jyväskylä is included in this thesis and discussed at the end of the second section.

These studies were carried out between 1996–2000 at the Department of Physics of the University of Jyväskylä. Complete results of this work are published in the enclosed articles listed below:

1. Transport of ions in ion guides under flow and diffusion

K. Peräjärvi, P. Dendooven, J. Huikari, A. Jokinen, V. S. Kolhinen, A. Nieminen, J. Äystö, Nuclear Instruments and Methods in Physics Research A 449 (2000) 427.

https://doi.org/10.1016/S0168-9002(99)01449-7

2. Investigation of a gas-catcher/ion guide system using alpha decay recoil products

K. Peräjärvi, J. Huikari, S. Rinta-Antila, P. Dendooven, Nuclear Physics A, in press.

3. Measurement of the IAS resonance strength in ^{23}Mg

K. Peräjärvi, T. Siiskonen, A. Honkanen, P. Dendooven, A. Jokinen, P. O. Lipas, M. Oinonen, H. Penttilä, J. Äystö, Physics Letters B 492 (2000) 1.

4. The $1^+ \rightarrow 0^+$ Gamow-Teller strength of the ^{58}Cu$_{g.s.} \rightarrow {}^{58}Ni_{g.s.}$ transition

K. Peräjärvi, P. Dendooven, M. Górska, J. Huikari, A. Jokinen, V. S. Kolhinen, M. La Commara, G. Lhersonneau, A. Nieminen, S. Nummela, H. Penttilä, E. Roeckl, J. C. Wang, J. Äystö, submitted to Nuclear Physics A.

2. Studies of Ion Transport in Gases

2.1. Introduction to the ion guide technique

In the conventional IGISOL system, reaction products are thermalized in a helium-filled gas cell and, using gas flow, guided through the exit hole to a vacuum chamber. The pressure difference needed to induce the flow is accomplished with a Roots blower unit. With the present configuration the effective pumping speed of the gas cell is over 3000 m^3/h [Pen97]. In the standard setup, we have an exit hole of 1.2 mm diameter and the gas-cell pressure is set somewhere between 10 and 50 kPa. These settings produce roughly a 100 Pa pressure in the vacuum chamber close to the exit hole. An essential point in this scheme is that it relies on the survival of ions in the gas, thus making re-ionization unnecessary. It is important that usually a major fraction of ions are in charge state +1 when entering the vacuum chamber. Recoils that survive evacuation as ions are separated from the neutral gas and accelerated using static electric fields and differential pumping. In the first step of this separation (between the nozzle and skimmer, see Fig. 2.1) the electric field gradient is kept rather low, at 10–400 V/cm, to be able to maintain reasonable beam quality, characterized by the mass resolving power $R = M/\Delta M = B_{max}/\Delta B_{FWHM} \approx 300$. Here M is the mass of the beam particles and B is the magnetic flux density. At the end of the acceleration, the +1 ions have about 40 keV of kinetic energy. Figure 2.1 illustrates more precisely how the acceleration is done.

Accelerated ions are mass separated with a dipole magnet. The mass-separated beam is implanted into a movable tape which is viewed with a set of detectors in optimum geometry. The vacuum after acceleration is usually in the 10^{-5} Pa region. It is maintained with diffusion and turbomolecular pumps.

The first on-line target/stopping chambers were designed for light-ion fusion-evaporation reactions. Their stopping volumes are only of the order of 1 cm^3. That is mainly because the primary beam travels through the stopping volume and ionizes the stopping gas creating a plasma, which increases the recombination rate. It is also important to note that

5

heavy nuclides (A ≈ 200) recoiling out of the target thermalize even in this small gas volume. However, with lighter nuclides only a small fraction of the target thickness is effectively used.
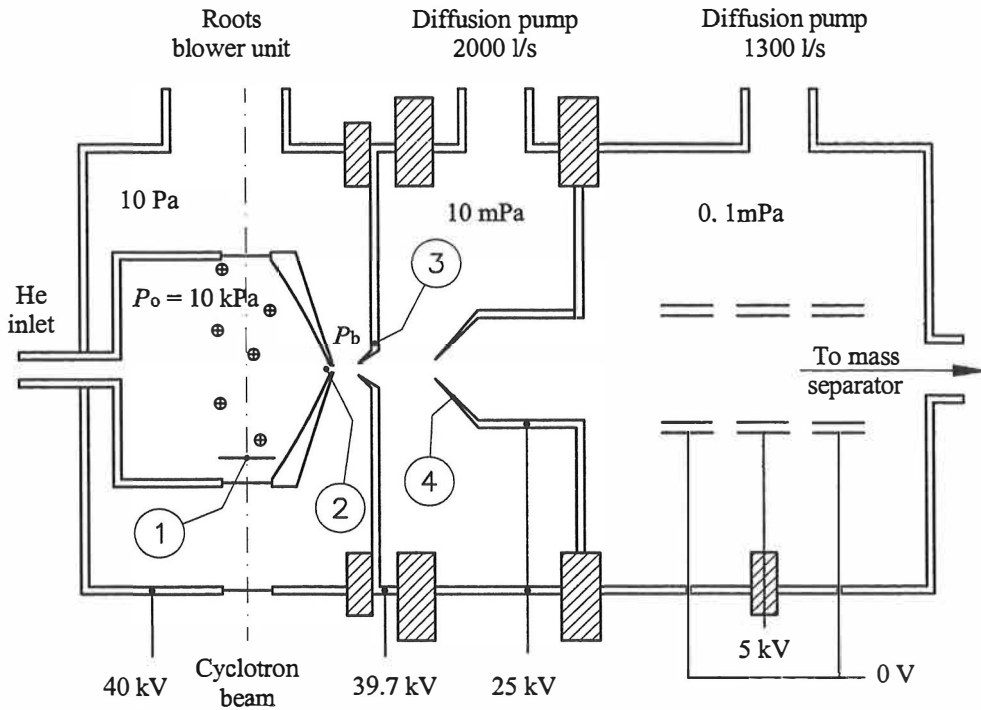
Fig. 2.1. Schematic drawing of the IGISOL system. Components of the system are: 1) target, 2) exit hole, 3) skimmer electrode and 4) extractor electrode.

The first version of a special double-chamber ion guide for proton-induced fission was introduced in 1989 [Tas89]. Separation of the target and stopping chamber is possible because of the nature of the fission reaction. This development made it possible to increase the size of the stopping volume (currently about 60 cm^3). However, the total efficiency of such a system, as measured with a 16.4 μA, 25 MeV proton beam is rather modest, only about 0.016% [Den98a]. The main problems are inadequate thermalization and rapid neutralization of fragments in the He gas.

In 1998, a chamber designed for heavy-ion fusion-evaporation reactions [Bér94] was connected to the Jyväskylä IGISOL facility. This method is based on the difference of angular distributions between reaction products and the primary beam after passing through a thick target (a few mg/cm^2). This observation again made it possible to separate the primary beam and the stopping volume from each other and increase the size of the stopping volume. In the first successful test, 0.5% of the reaction products entering the buffer gas were transported to the measuring area independently of the primary beam intensity [Den98b].

2.2. Macroscopic flow conditions

Although the IGISOL technique is nearly twenty years old and adopted by several laboratories around the world, the processes responsible for the performance of the ion guide are not well understood even at low beam intensities. In the following pages we approach this problem from a fluid-dynamical point of view and develop a method to compute the macroscopic flow field of a typical IGISOL gas cell.

In a standard IGISOL system, the critical pressure condition

$$\frac{P_0}{P_b} \geq \left(\frac{\gamma+1}{2}\right)^{\frac{\gamma}{\gamma-1}} \tag{2.2.1}$$

is fulfilled. Here P_0 is the pressure inside the target chamber and P_b the background pressure in the vacuum chamber (see Fig. 2.1); γ is c_p/c_v, where c_p is the specific heat at constant pressure and c_v the specific heat at constant volume. For He the value of γ is 5/3. While this critical pressure condition is fulfilled, the mean velocity of flow at the throat of the nozzle is equal to the speed of sound in the buffer gas and continues to accelerate until the normal shock disk is reached. The average position of the shock disk x_{ave} in mm can be predicted with the empirical formula [Ras96]

$$x_{ave} = 0.88\phi\left(\frac{P_0}{P_b}\right)^{1/2} \tag{2.2.2}$$

7

where ϕ is the diameter of nozzle in mm.

Due to the utmost importance of this pressure ratio to our simulations, we wanted to study and verify it experimentally. This was done by studying the delayed part of the light emitted by a standard discharge source [Ras96]. Pictures were taken with a PCO Sensi Cam CCD-camera [PCO98] with a 3 ms exposure time. As an example of the results, a flow structure with $P_0 = 20$ kPa is presented in Fig. 2.2.
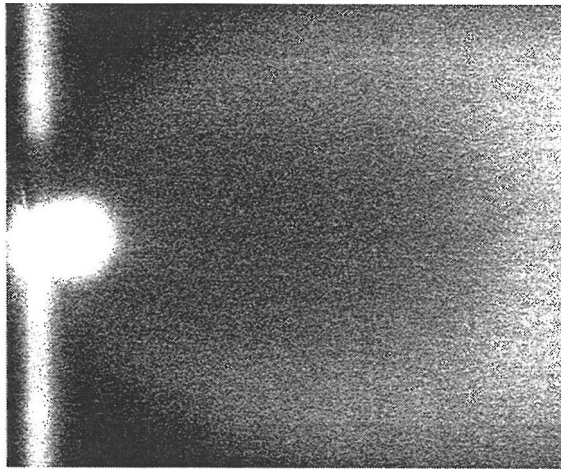

Fig. 2.2. Free-jet expansion in standard pumping conditions. The exit hole ($\phi = 1.2$ mm) is in the middle on the left side and the normal shock disk is seen as a bright area on the right. Bright areas at the top and bottom are formed between the jet boundary and the barrel shock.

A shock structure is clearly seen in Fig. 2.2, which means that the critical pressure ratio is well over 2.05 (critical pressure ratio for He). Shock structures were seen in all measurements throughout the interesting pressure range. Therefore we may conclude that the mean velocity of flow at the throat of the nozzle is equal to the speed of sound in the gas, independent of gas cell pressure. In a real setup, the skimmer plate is situated next to the nozzle (see Fig. 2.1). Usually the distance between the nozzle and the skimmer is so small (about 1 cm) that the skimmer has a crucial effect on the flow pattern in the vacuum chamber. Figure 2.3 gives an idea of the disturbance related to the skimmer in a

realistic IGISOL setup. The skimmer plate in Fig. 2.3 is at the same electrical potential as the discharge chamber.
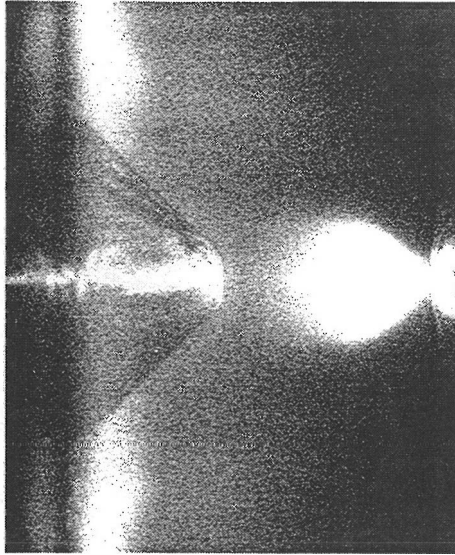

Fig. 2.3. Free-jet expansion when a standard skimmer is introduced. The pressure P_0 is 78 kPa. The exit hole is now in the middle on the right and the skimmer is on the left.

Already during subsonic acceleration inside the target chamber, the temperature starts to decrease, which means that the thermal motion is converting to ordered translational motion. It also means that we have to consider compressible flow near the exit hole. On the other hand, in the main part of the target chamber, the Reynolds number $\rho v L/\mu$ and Mach number v/c are relatively small, indicating that there the flow should be treated as laminar and incompressible. Here ρ is the density of the gas, v the velocity of the flow, L the diameter of the flow channel, μ the viscosity and c the velocity of sound in the medium. A situation like this is difficult to simulate since the nature of the flow changes dramatically in the middle of the computation region. The main difference between these regions is that in the incompressible region the pressure cannot be straigthforwardly coupled to density. To keep our model simple and effective we overcame this difficulty by approximating the flow near the exit hole as a steady, isentropic, quasi-one-

9

dimensional, compressible flow of an ideal gas [And90] and then treating the rest of the flow as incompressible.

2.3. Steady isentropic quasi-one-dimensional compressible flow

As was shown in the last section, the average velocity of flow is equal to the speed of sound c at the throat of the nozzle. This means that the Mach number is equal to unity at the throat. Flow is commonly defined to be compressible if the Mach number is over 0.3. In our case this is true only in the vicinity of the exit hole inside the converging nozzle. For simplicity, we treat the flow in that region as isentropic and quasi-one-dimensional. This means that we neglect heat transfer and friction and consider the flow properties as constant across any given cross-sectional area of the nozzle. The cross-sectional area A is treated as an independent variable. After some algebra we get the following relationship between the cross-sectional area A and Mach number M [And90]:

$$\frac{A}{A^*} = \frac{1}{M}\left[\frac{1+(\gamma-1)M^2/2}{1+(\gamma-1)/2}\right]^{\frac{\gamma+1}{2(\gamma-1)}} \qquad (2.3.1)$$

where A^* is the cross-sectional area of the exit hole. The macroscopic flow quantities temperature (T), pressure (P) and density (ρ) in a certain plain close to the nozzle exit are related to the Mach number according to

$$T = \frac{T_0}{1+(\gamma-1)M^2/2} \qquad (2.3.2)$$

$$P = \frac{P_0}{\left[1+(\gamma-1)M^2/2\right]^{\frac{\gamma}{\gamma-1}}} \qquad (2.3.3)$$

$$\rho = \frac{\rho_0}{\left[1+(\gamma-1)M^2/2\right]^{\frac{1}{\gamma-1}}} \qquad (2.3.4)$$

where T_0, P_0 and ρ_0 are the stagnation values for different flow properties. In practical terms, they are roughly the measured gas temperature, pressure and density. The average flow properties at the throat of the nozzle can be calculated from Eqs. (2.3.2)–(2.3.4) by setting M equal to one. A formula can also be derived for the total mass-flow rate dm/dt:

$$\frac{dm}{dt} = P_0 A^* \sqrt{\frac{\gamma}{WT_0}\left(\frac{2}{\gamma+1}\right)^{\frac{\gamma+1}{\gamma-1}}} \tag{2.3.5}$$

where $W = (8314.4/ \text{atomic mass number})$ J/kgK. Equation (2.3.5) is used to produce a formula for the conductance C_e [l/s] of an incompressible gas through the whole system (note that $P_0 = \rho_0 WT_0$):

$$C_e = \frac{dm/dt}{\rho_0} = \frac{\pi}{4000}\sqrt{\gamma WT_0\left(\frac{2}{\gamma+1}\right)^{\frac{\gamma+1}{\gamma-1}}}\,\phi^2 \approx 0.45\phi^2 \tag{2.3.6}$$

The approximate numerical value given on the right hand side of Eq. (2.3.6) is for He; T_0 was set to 295 K and ϕ is the diameter of the nozzle in mm. Exactly this same relation for He conductance can be extracted from the measurements.

With the quasi-one-dimensional model we extrapolate the pressure from the throat of the nozzle upstream into a certain plain and use this plain as a pseudo throat of the nozzle in the main computation. Extrapolation is naturally done far enough upstream that we are allowed to use incompressible equations in the main computation ($M < 0.3$).

2.4. Three-dimensional incompressible flow

In the region of incompressible flow we have four unknowns, the three velocity components and the pressure, which can be determined by solving the Navier–Stokes equations [Tan97]

$$\nabla \cdot \mathbf{v} = 0 \tag{2.4.1}$$

$$\nabla \cdot \left(\rho \mathbf{v} \mathbf{v} - 2\mu \mathbf{\Pi} \right) = -\nabla P \qquad (2.4.2)$$

The components of the dyad $\mathbf{\Pi}$ are given by

$$\Pi_{ij} = \frac{1}{2}\left(\frac{\partial v_i}{\partial x_j} + \frac{\partial v_j}{\partial x_i} \right), \; (i, j) = 1, 2, 3 \qquad (2.4.3)$$

Instead of solving Eqs. (2.4.1) and (2.4.2), we consider the global integral equations

$$\int_{CS} \mathbf{v} \cdot d\mathbf{A} = 0 \qquad (2.4.4)$$

$$\int_{CS} \left(\rho \mathbf{v} \mathbf{v} + P\mathbf{I} - 2\mu \mathbf{\Pi} \right) \cdot d\mathbf{A} = 0 \qquad (2.4.5)$$

(CS means control surface). These equations are solved by using the commercially available codes CFX 4.2 [AEA94] and FLUENT 5 [Flu98]. This is done by dividing the total integration volume into smaller cells, and by applying Eqs. (2.4.4) and (2.4.5) to each of these partial volumes. Then the equations are discretized so that the flow velocities and pressure are approximated to have constant values at each point on a certain cell surface. All except the advection terms are discretized by using the central difference between the midpoints of neighbouring cells. The advection terms are computed by using the van Leer difference scheme [Tan97, AEA94]. The coupling between pressure and velocity is handled with the SIMPLEC algorithm, which connects pressure to velocity in such a way that mass is conserved [Tan97, AEA94]. When computing with incompressible equations, one usually fixes the velocity field at the inlet and the static pressure at the outlet. The inlet velocities are calculated from the mass flow rate given by the quasi-one-dimensional model. No slip-wall boundary conditions are used for solid surfaces.

As an example, a flow profile of a typical light-ion fusion-evaporation target chamber is presented in Fig. 2.4. Helium was used as a buffer gas and the target chamber pressure was set to 10 kPa. The diameter of the nozzle was 1.2 mm.
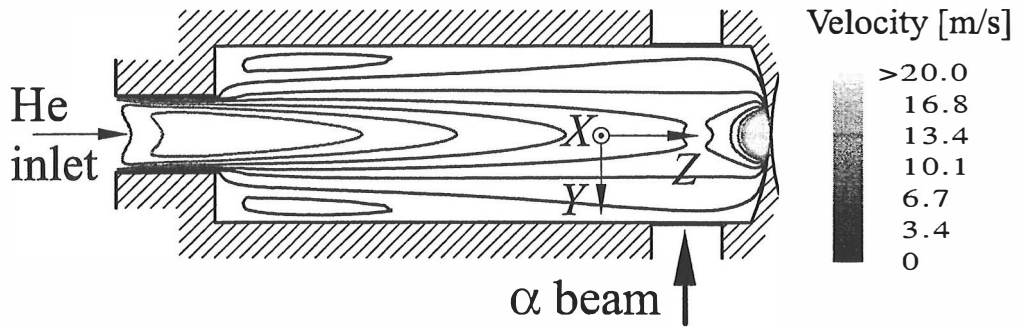
Fig. 2.4. IGISOL target chamber and a contour plot of its flow pattern.

One should notice that there can be mass transfer between the flow particles. Therefore standard fluid dynamics only describes the macroscopic movement of the gas. On the other hand, in the ion guide the number of interesting ions is small compared to the number of neutral gas particles. Therefore the next step is to study the motion of single ions in a flowing buffer gas.

2.5. The role of thermal motion

For simplicity, let us first assume an extended constant-velocity gas-flow field, where we place some particles (atoms or ions) in a line perpendicular to the flow direction, later called the creation line, and follow their distribution as a function of time. The global maximum of the distribution always remains at the creation line which moves with a macroscopic flow velocity v_f. Therefore one might expect that the local maximum in a certain plain perpendicular to the flow direction, a distance d downstream from the creation line, is reached when the macroscopic flow has transported the creation line to that distance. But due to diffusion, this conclusion is not true. This can be shown quantitatively by solving the generalized diffusion equation [Atk90]

$$\frac{\partial n}{\partial t} = D \frac{\partial^2 n}{\partial x^2} - v_f \frac{\partial n}{\partial x} \qquad (2.5.1)$$

where D is the diffusion constant. A particular solution is

$$n(x,t) = \frac{1}{\sqrt{t}} \exp\left[-\frac{(x - v_f t)^2}{4Dt} \right] \qquad (2.5.2)$$

By setting $x = d$ and the time derivate of $n(x,t)|_{x=d}$ equal to zero, we get a relation for the most probable transport time t_e to a distance d downstream from the creation line as a function of flow velocity and diffusion constant (see Eq. 2.5.3 and Fig. 2.5):

$$t_e = -\frac{D}{v_f^2} + \sqrt{\frac{D^2}{v_f^4} + \frac{d^2}{v_f^2}} \qquad (2.5.3)$$

A basic assumption in this derivation is that v_f is much smaller than the average velocity of particles between random collisions, resulting only in a small disturbance in collisional equilibrium. Note that if $D = 0$, then t_e collapses to d/v_f.
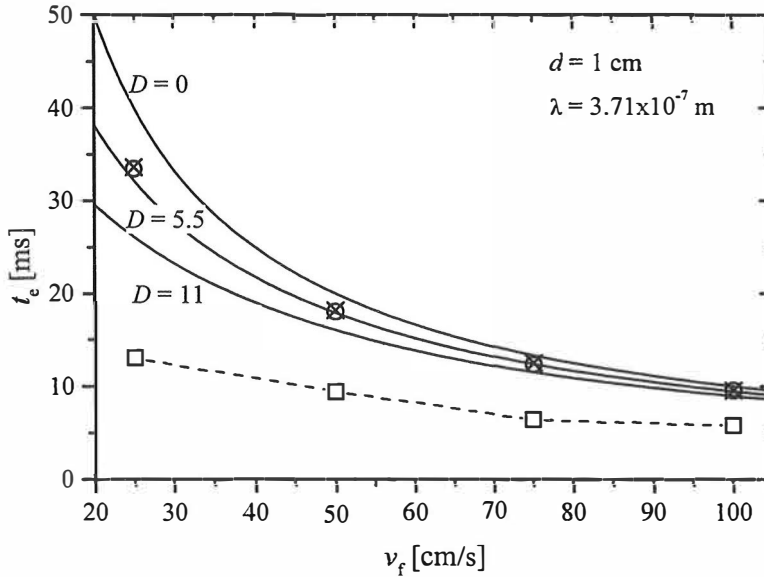
Fig. 2.5. The most probable evacuation time t_e (solid lines, circles and crosses) as a function of macroscopic flow velocity v_f. The solid lines are plots of Eq. (2.5.3). The open circles are computed without scaling and the crosses with scaling; see the text. The diffusion constant D is 5.5 cm^2/s in both cases. The open squares correspond to the times when the first particles travel through the detection plane, computed with $D = 5.5$ cm^2/s.

To demonstrate the role of diffusion suggested by Eq. (2.5.3) let us chose $v_f = 25$ cm/s and $D = 5.5$ cm^2/s and plot $n(x,t)$ at two different times (see Fig. 2.6): $t = 40$ ms, when the global maximum is at $d = 1$ cm, and at 32.16 ms. As we can see from Fig. 2.6, the earlier time gives a higher local intensity at 1 cm, which is exactly what Eq. (2.5.3) suggests.
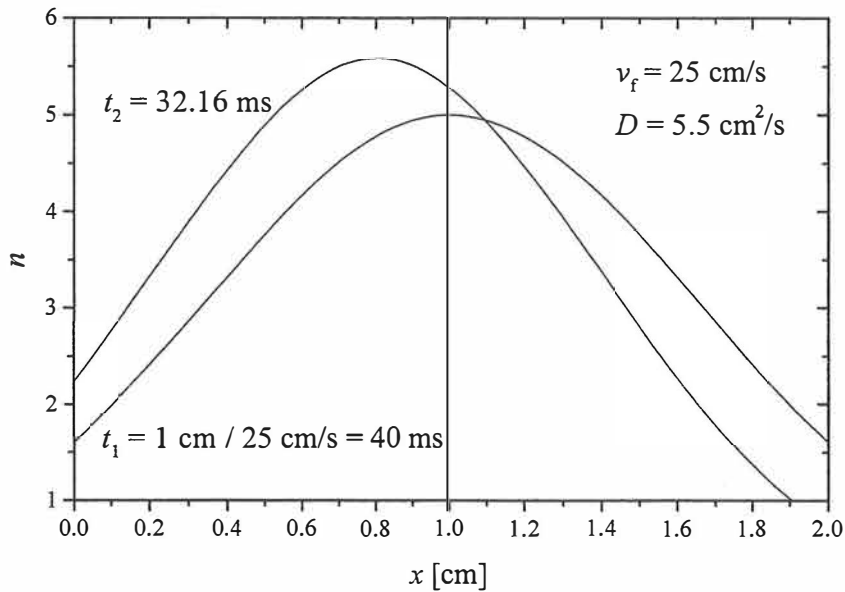
Fig. 2.6. Particle number density as a function of the distance from the original creation line at two instants of time.

It is also important to note that the evacuation time of a single gas particle cannot be predicted exactly due to the random nature of thermal motion. In the case of a more complicated flow field, where particles can diffuse to faster or slower regions of the chamber, the role of thermal motion can be even more important. In more realistic cases one has to rely on numerical simulations.

2.6. A unified model for ion transportation in ion guides under flow and diffusion

The Einstein–Smoluchowski relation [Atk90], Eq. (2.6.1), can be used to provide a bridge between the macroscopic and microscopic pictures:

$$D = \frac{\lambda^2}{2t_c} \qquad (2.6.1)$$

A numerical value for D can be interpolated from the existing experimental data [Vie95]. The quantity λ is the mean free path between random collisions. It can be calculated using the kinetic theory of gases [Fon86]:

$$\lambda_{ab} = \frac{4kT}{\pi P (\xi_a + \xi_b)^2 (1 + m_a / m_b)^{1/2}} \qquad (2.6.2)$$

This equation holds when the number of interesting particles a is small compared to the number of buffer gas particles b. In Eq. (2.6.2) k is Boltzmann's constant, T the temperature, ξ the diameter of particles and m their mass. The average time t_c between random collisions can then be calculated using Eq. (2.6.1). Both λ and t_c are needed as input parameters in the simulation. They are kept constant during a computation. Only the direction of the step λ is randomly selected at the beginning of each new loop in the program. The macroscopic flow and the random motion are combined at the beginning of each new loop according to

$$\lambda_{new} = \lambda_{old} + \mathbf{v}_f(x, y, z)t_c \qquad (2.6.3)$$

A relatively accurate macroscopic velocity field is needed as an input for these simulations. The macroscopic flow field is computed using the model introduced earlier. The total evacuation time for a particle is t_c times the number of loops needed to transport the particle out of the stopping chamber. This method is based on the same assumptions that were already used in the constant-velocity case. Major improvements of this approach are that it is not bound to simple ion distributions and constant flow velocity.

In Fig. 2.5, the results obtained by this approach in the case of a constant-velocity gas-flow field with $D = 5.5$ cm^2/s (open circles) are compared with the analytical solution (2.5.3). The open squares in Fig. 2.5 correspond to the times when the first particles arrive at the distance d downstream from the creation line. These times depend on the

number of particles used in the simulation. To keep the CPU time at a reasonable level, in more realistic cases λ is multiplied by 10 and t_c by 100. This kind of scaling does not change D. Results with scaled λ and t_c in this test case are plotted in Fig. 2.5 as crosses. Computed results with and without scaling agree fairly well with the analytical solution. Usually only 1000–5000 particles were used in one simulation. All of them were created and transported at the same time.

With realistic geometries, particles touching the chamber wall are removed from the simulation because ions touching the wall are neutralized.

2.7. Comparison between simulations and measurements

Delay-time measurements made in Leuven with stable Ni ions [Qam94] are used here to test the simulation model. A nickel filament (see Fig. 2.7) was used to produce the Ni atoms needed in the He gas flow.
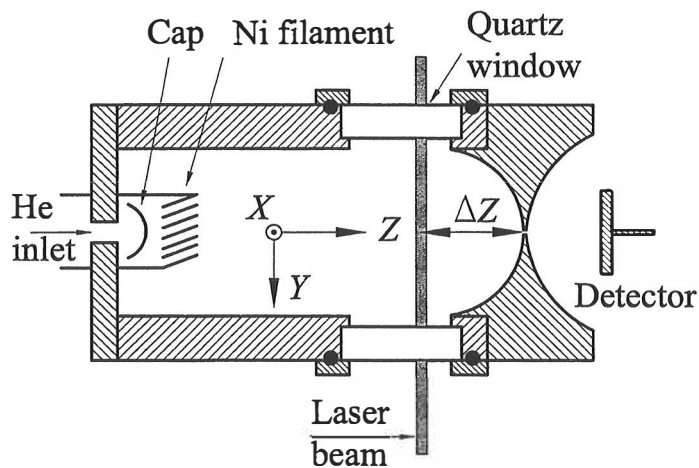

Fig. 2.7. Schematic picture of the chamber used in the ionization measurements. The diameter of the exit hole is 0.5 mm and the radius of the nozzle's curvature is 10 mm.

Some of the sublimated Ni atoms were then ionized selectively using monochromatic (322.698 nm) two-step laser-resonance ionization. In their setup, the pulsed ionizing laser beam entered from the side of a cylindrically symmetric chamber as shown in Fig. 2.7.

The Ni ions which were transported out of the ionization chamber by the He flow were detected with a negatively biased detector. The ion intensity versus time since the laser was fired was recorded. When analyzing the measured time distributions, the flight time between the exit hole of the gas cell and the detector was considered to be negligible. Twenty-one separate ionization measurements were made using a He pressure of 10 kPa. The results are shown in Fig. 2.8.
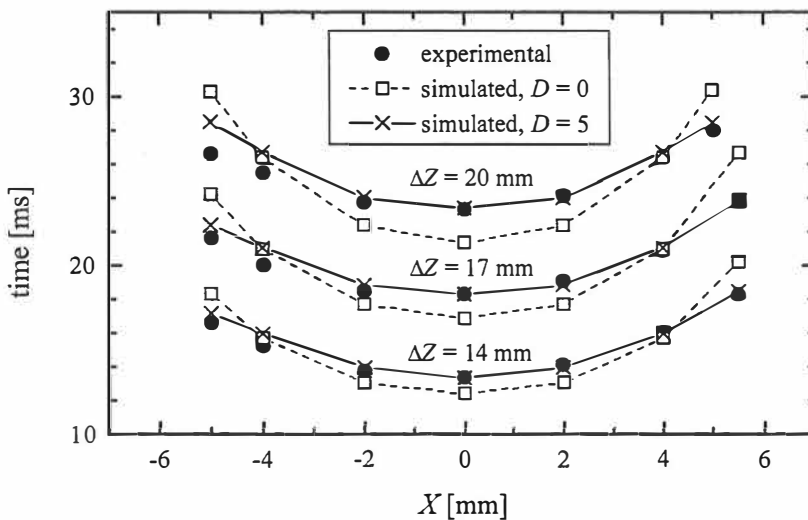
Fig. 2.8. Measured and computed most probable evacuation times for different $(\Delta Z, X)$ combinations. Definitions for ΔZ and X are given in Fig. 2.7.

In our simulations, ions were created randomly along the lines where ionization occurred in the experiments. In the experimental setup, the distribution of Ni atoms is not constant along the ionization line. Because we do not know the exact initial distribution of Ni atoms sublimated from the filament, there is no reason to try to simulate the transport of atoms from their creation site to their ionization zone. However, with the setup used (Fig. 2.7), the density of Ni atoms is the highest in the volume close to the cylindrical

symmetry axis of the chamber (Z axis in Fig. 2.7). From there on, it decreases towards the walls. The effect of this can be seen in Fig. 2.9 where the measured and computed time distributions are compared. The long tails in the simulated curves are due to the assumed homogeneous ion distribution. This conclusion is confirmed in [Kud96]. From our point of view, the important fact is that the difference in initial distribution does not influence the beginning of the evacuation time distribution. This is because the fastest ions coming out of the gas cell are mainly created in the macroscopically fastest part of the ionization line, where the ion density also has its maximum and where the ion density can be approximated to stay nearly constant. This maximum ion density in reality corresponds to our constant density in the simulation.
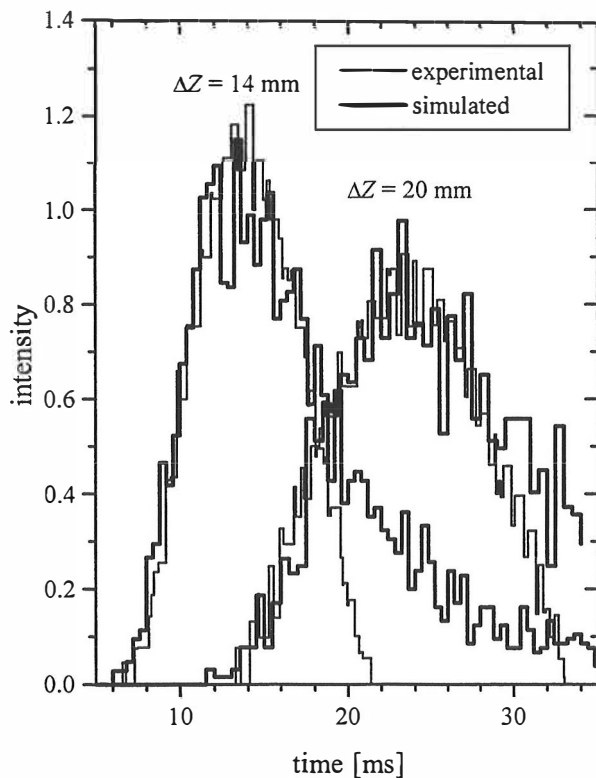

Fig. 2.9. Simulated and measured evacuation time profiles for $\Delta Z = 14$ and 20 mm and $X = 0$ mm (Fig. 2.7).

When determining the most probable evacuation times for ions, the long tails shown in Fig. 2.9 were excluded. The number density $n(x,t)$ given by Eq. (2.5.2), multiplied by a constant, was used to fit the data. With this approach one can reproduce the most probable experimental evacuation times quite well, as can be seen in Fig. 2.8 ($D = 5$). The most probable evacuation times given by standard fluid-dynamical simulation ($D = 0$) are also presented in Fig. 2.8. The role of thermal motion as a transport mechanism of ions is macroscopically seen as a shift of the most probable evacuation times from the standard fluid-dynamical ones. The thermal motion delays the faster part and speeds up the slower part of the chamber. The role of the thermal motion is also seen in the width of the evacuation time distribution. With the macroscopic model, distributions are always too narrow close to the maximum as compared with the experimental ones. Naturally, the long tail of the distribution due to the initial condition is also seen in the macroscopic solution. Numerical values of the parameters used in the simulations are given in Table 2.1.

Table 2.1. Numerical values of the parameters used in the simulations.

Parameter	Value
Stagnation pressure (He)	10 kPa
Stagnation temperature	295 K
D	5.0 cm^2/s
λ	3.57×10^{-7} m
λ scaling factor	10

In the resonance-ionization measurements described, the time behaviour of the ion signal was unchanged when the laser energy was changed from 0.5 to 1.5 mJ [Qam94]. This indicates that the ion concentration in the experimental conditions was so low that Coulomb repulsion between Ni ions could be neglected. This was also assumed in the model.

Because of the axial symmetry of the chamber (Fig. 2.7) one would expect that the experimental values (Fig. 2.8) are the same for, say, $X = +5$ mm and $X = -5$ mm.

However, a slight asymmetry is seen in Fig. 2.8. This asymmetry is probably due to offset in placing the Ni filament. This conclusion is supported by the fact that the farther one goes from the filament, the better our approximation works.

The remainder of the theoretical and experimental results of this work concerning gas catchers and ion guides can be found in Publications 1 and 2.

3. Nuclear Spectroscopy Applications

3.1. Relevant aspects of nuclear physics

From the standard nuclear physics point of view the atomic nucleus is composed of nucleons (protons and neutrons). The nucleon–nucleon strong interaction that binds nuclei is charge independent and has a short range, only about 2 fm. Properties of nuclei with $A > 2$ cannot be calculated exactly because of many-body complications that increase rapidly with A. The nuclear Hamiltonian has the form

$$H = \sum_{k=1}^{A} T(k) + \sum_{1=k<l}^{A} W(k,l) \tag{3.1.1}$$

where $T(k)$ is the kinetic energy of nucleon k and $W(k,l)$ the two-body interaction between nucleons k and l. To overcome computational problems, various simplified models have been developed to treat the nuclear many-body problem. The most standard of them is the nuclear shell model which is sketched in the following section.

3.1.1. Nuclear shell model

To get into the shell-model approximation we add and subtract a single-particle potential term $U(k)$ in Eq. (3.1.1) and rearrange the terms:

$$H = \sum_{k=1}^{A} [T(k) + U(k)] + \left[\sum_{1=k<l}^{A} W(k,l) - \sum_{k=1}^{A} U(k) \right] = H^{(0)} + H^{(1)} \tag{3.1.2}$$

The $H^{(0)}$ part of the Hamiltonian describes nucleons moving independently in the average potential produced by the other nucleons. The eigenstates of $H^{(0)}$ are orthonormal A-body states Φ_n with energies

$$E_n^{(0)} = \sum_i \nu_{ni} \varepsilon_i \tag{3.1.3}$$

where the ε_i are the single-particle energies and the ν_{ni} are their occupations in the many-particle state Φ_n. The term $H^{(1)}$ in Eq. (3.1.2) is the residual interaction. If the single-particle potential is well calculated or chosen, $H^{(1)}$ is so small that it can be treated as a perturbation. This perturbation causes mixing of A-body states which are close in energy and have the same quantum numbers. The wave functions Ψ_n with $H^{(1)}$ taken into account are linear combinations of the states, Φ_n:

$$\Psi_n = \sum_{n'=1}^{g} a_{nn'} \Phi_{n'} \qquad (3.1.4)$$

From g orthonormal A-body states Φ_n one can construct g orthonormal states Ψ_n. The coefficients $a_{nn'}$ are determined by solving the Schrödinger equation $H\Psi_n = E_n \Psi_n$.

Beyond the lightest nuclei, one cannot take into account all nucleons present in the nucleus. Instead one assumes that there is an inert core, often a doubly magic nucleus, which only contributes to the mean field of the valence nucleons. Only the interactions between the valence nucleons are treated explicitly. Valence nucleons are mainly responsible for properties of nuclei at low excitation energies. The model space from which the states Φ_n are constructed has to be restricted to a reasonable size due to finite computing resources.

Often shell-model calculations are done by assuming that the proton and neutron are two states of the nucleon, and the projection M_T of the isospin quantum number T tells the charge state of the nucleon. The quantum number M_T is $-1/2$ for the proton and $+1/2$ for the neutron. This simplification produces identical single-particle states for protons and neutrons. The total M_T for a nucleus is $(N-Z)/2$, where N is the neutron number and Z the proton number. In most cases the isospin T of the ground state is equal to $|M_T|$.

3.1.2. *Nuclear beta decay*

Beta decay provides one way for a nucleus to proceed towards its minimum energy. In the context of this work only allowed beta decay needs to be considered. Allowed beta decay can be divided into Fermi and Gamow–Teller parts.

In pure Fermi beta decay the initial and final states have the same spin and parity J^π. Isospin T remains unchanged in Fermi beta decay, but its orientation is changed by one unit, $\Delta M_T = \pm 1$. The squared Fermi matrix element is model independently [Bru77]

$$\langle M_F \rangle^2 = T(T+1) - M_{Ti} M_{Tf} \tag{3.1.5}$$

In allowed Gamow–Teller beta decay the angular momentum selection rule is $\Delta J = 0, \pm 1$ and the parity remains unchanged. For example, Gamow–Teller beta decay from the $J^\pi = 5/2^+$ ground state of ^{23}Al can proceed only to ^{23}Mg states which have $J^\pi = 3/2^+$, $5/2^+$ or $7/2^+$. The isospin selection rules for Gamow–Teller beta decay are $\Delta T = 0, \pm 1$ and $\Delta M_T = \pm 1$. The squared Gamow–Teller matrix element can be expressed as [Bru77, Hon97]

$$\langle M_{GT\pm} \rangle^2 = \frac{1}{2(2J_i+1)} \begin{pmatrix} T_f & 1 & T_i \\ -M_{Tf} & \pm 1 & M_{Ti} \end{pmatrix}^2 \left(\alpha_f J_f T_f \;\|\|\; \sum_{k=1}^{A} \sigma(k)\tau(k) \;\|\|\; \alpha_i J_i T_i \right)^2 \tag{3.1.6}$$

The triple-barred quantity in Eq. (3.1.6) is a matrix element reduced both in mechanical space and in isospin space. The + sign refers to β^+ decay and the − sign to β^- decay.

Experimental observables and Fermi and Gamow–Teller matrix elements are related according to [Kan95]

$$f(1+\delta_R)t_i = \frac{C}{\langle M_F \rangle^2 (1-\delta_C) + \left(\dfrac{g_A}{g_V} \right)^2 \langle M_{GT} \rangle^2} \tag{3.1.7}$$

The partial half-life t_i is equal to $t_{1/2}/b_i$, where $t_{1/2}$ is the total half-life and b_i the branching ratio for the transition i. Numerical values for the statistical rate function $f(Z, E_{max})$ can be

determined from [Gov71, Des87]. The quantity $(1 + \delta_R)$ is the radiative correction and $(1 - \delta_C)$ the Coulomb correction. For the constant C we adopt the value 6145(4) s [Tow95]. The quantity g_A is the axial-vector coupling constant and g_V the vector coupling constant. For the ratio $|g_A/g_V|$ we adopt the value 1.266(4) [Sch95a]. In Publications 3 and 4 the Fermi transition strength $B(F)$ is equal to $\langle M_F \rangle^2$ and the Gamow–Teller transition strength $B(GT)$ is defined as

$$B(\mathrm{GT}) = \left(\frac{g_A}{g_V} \right)^2 \langle M_{GT} \rangle^2 \tag{3.1.8}$$

3.2. Beta decay of ^{23}Al

Proton-rich nuclei with isospin $T \geq 3/2$ provide unique opportunities to study beta decay strength over a wide energy interval. The relevant odd-Z nuclei have not been studied much, due to the weak charged-particle decay channels, low production cross sections and short beta half-lives. The best-studied case in this series is ^{35}K [Ewa80].

This thesis work includes a detailed study of the $M_T = -3/2$ nucleus ^{23}Al (Publication 3). The isotope ^{23}Al was produced via the ^{24}Mg(p,2n) reaction at 40 MeV beam energy and mass-separated using the IGISOL system. The mass-separated ion beam was implanted into a thin carbon foil which was viewed by an HPGe detector, a 1 mm thick plastic ΔE_β detector and a gas ΔE-Si E detector telescope (see Fig. 3.1).

Fermi decay from the $5/2^+$ ground state of ^{23}Al leads to the isobaric analogue state (IAS) in ^{23}Mg which is known to be proton unbound [Aud95]. Beta-delayed proton decay of ^{23}Al has been reported previously [Gou72, Tig95], but without observation of gamma rays. Proton emission from the IAS has been reported by Tighe et al. [Tig95]. The deduced proton branching $b_p = 3.5(19)\%$ suggested large isospin mixing for the IAS. This value is partly based on a calculated cross section and it strongly disagrees with the full 1s0d configuration shell-model calculation which includes isospin mixing of the IAS.
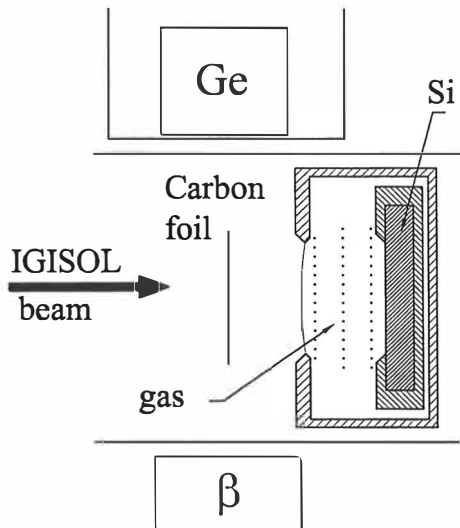
Fig. 3.1. Measurement setup used in the [23]Al work.

In our work the $T = 3/2$ isobaric analogue state, at 7801(2) keV, was observed for the first time to decay by both proton and gamma emission, with a proton branching of 0.17(8)%. By adopting the gamma decay width of 3.0(2) eV [End90] measured for the lowest $T = 3/2$ (mirror) state in [23]Na as the total width of the IAS in [23]Mg, we were able to deduce the proton and gamma widths for the IAS in [23]Mg. Thus we found $\Gamma_p(\text{IAS}) = 5(2)$ meV and $\Gamma_\gamma(\text{IAS}) = 3.0(2)$ eV. Other spectroscopic results of this work are reported in Publication 3.

The decay properties of the IAS in [23]Mg have astrophysical significance, since its proton and gamma widths make important contributions to the hot NeNa cycle [Jos99]. The reaction [22]Na(p,γ)[23]Mg, involved in the hot hydrogen-burning NeNa cycle (see Fig. 3.2), is important for predicting nuclear burning rates at high temperatures (about 10^8 K).
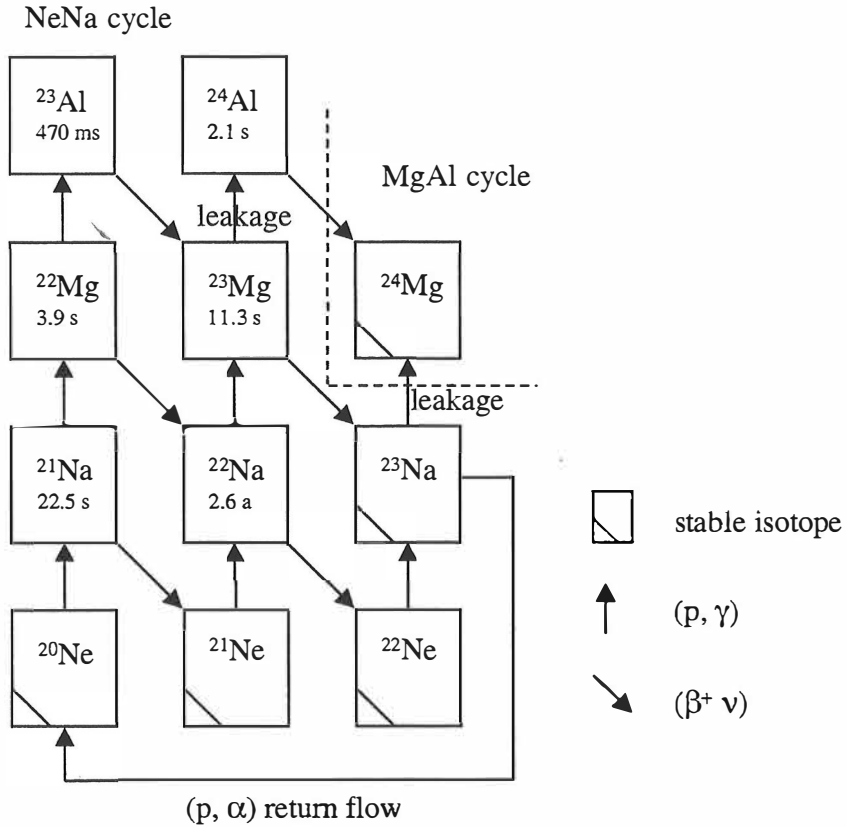
NeNa cycle

^{23}Al 470 ms	^{24}Al 2.1 s	
^{22}Mg 3.9 s	^{23}Mg 11.3 s	^{24}Mg
^{21}Na 22.5 s	^{22}Na 2.6 a	^{23}Na
^{20}Ne	^{21}Ne	^{22}Ne

leakage

MgAl cycle

leakage

stable isotope

(p, γ)

$(\beta^+ \nu)$

(p, α) return flow

Fig. 3.2. Hydrogen-burning NeNa cycle.

To which path the NeNa cycle proceeds depends on the temperature T. At low temperatures the path proceeds via stable nuclei as shown in Fig. 3.2. When T increases to a level where the proton-capture rate is able to compete with the beta decay rate in ^{22}Na $(T_{1/2} = 2.6$ a$)$ the NeNa cycle turns into the hot mode:

$$^{20}\mathrm{Ne}(\mathrm{p},\gamma)^{21}\mathrm{Na}(\beta^+\nu)^{21}\mathrm{Ne}(\mathrm{p},\gamma)^{22}\mathrm{Na}(\mathrm{p},\gamma)^{23}\mathrm{Mg}(\beta^+\nu)^{23}\mathrm{Na}(\mathrm{p},\alpha)^{20}\mathrm{Ne} \tag{3.2.1}$$
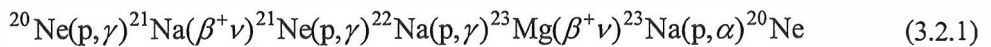
At what temperature this transition occurs depends also on the stellar density ρ. According to earlier data, at nova conditions $(\rho = 5 \times 10^3$ g/cm$^3)$ proton capture on ^{22}Na

starts to dominate when the temperature is about 4×10^7 K [Wie86]. When the temperature is further increased, up to about 1.2×10^8 K, proton capture on ^{21}Na starts to compete with beta decay [Wie86]. At this point the hot cycle takes the form

$$^{20}\text{Ne}(\text{p},\gamma)^{21}\text{Na}(\text{p},\gamma)^{22}\text{Mg}(\beta^+\nu)^{22}\text{Na}(\text{p},\gamma)^{23}\text{Mg}(\beta^+\nu)^{23}\text{Na}(\text{p},\alpha)^{20}\text{Ne} \qquad (3.2.2)$$
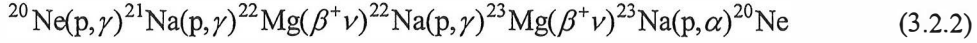
The only limiting factors in this cycle are the beta decay half-lives of ^{22}Mg and ^{23}Mg. Recent progress on the nuclear physics side [Ste96, Publication 3] improves the reaction-rate prediction for ^{22}Na(p,γ)^{23}Mg at around 10^8 K. We now recalculate this reaction rate in the temperature range from 9×10^7 to 5×10^8 K and compare it to the prediction given by [Sch95b] (see Fig. 3.3).

By assuming that resonances are isolated and narrow, which is true in the case of ^{22}Na(p,γ)^{23}Mg, the calculated thermonuclear reaction rate is [Cha92]

$$N_A \langle \sigma v \rangle = N_A \left(\frac{2\pi}{\mu k T} \right)^{3/2} \hbar^2 \left[\sum_i \omega \gamma_i \exp\left(-\frac{E_{ri}}{kT} \right) \right] \qquad (3.2.3)$$

where N_A is Avogadro's constant, μ the reduced mass, k Boltzmann's constant, and $\omega\gamma_i$ the strength and E_{ri} the energy of resonance i. The resonance strength $\omega\gamma$ is defined as [Wie86]

$$\omega\gamma = \frac{2J+1}{(2J_T+1)(2J_P+1)} \frac{\Gamma_p \Gamma_\gamma}{\Gamma_p + \Gamma_\gamma} \qquad (3.2.4)$$

where J is the spin of the final state produced, J_T and J_P are the spins of the target and projectile used in the resonance reaction experiment, and Γ_p and Γ_γ are the proton and gamma widths of the final state. The partial widths Γ_i are inversely proportional to partial mean lifetimes τ_i ($\Gamma_i = h/2\pi\tau_i$). In Eq. (3.2.3) the sum runs over all resonances and the result is given in units of $\text{m}^3\text{s}^{-1}\text{mole}^{-1}$. In the temperature range considered the reaction rate of ^{22}Na(p,γ)^{23}Mg is mainly determined by the three resonances at energies 213.3(27) keV [Ste96], 232(2) keV [Publication 3] and 287.9(21) keV [Ste96]. The deduced widths Γ_i for the IAS result in a resonance strength $\omega\gamma$ = 2.2(10) meV for the 232 keV

resonance when J_T is set to 3 (^{22}Na) and J_P to 1/2 (proton). This value is consistent with the upper limits from resonance reaction studies of proton capture on a radioactive ^{22}Na target, ≤ 1.3 meV [Seu90] and ≤ 2.6 meV [Ste96]. Table 3.1 gives the experimentally known resonances in ^{23}Mg with definitely measured resonance strengths. The first and third rows in Table 3.1 correspond to the resonances at 213 and 288 keV.

Table 3.1. Measured resonance strengths in ^{23}Mg.

E (keV)	J^π	$\omega\gamma$ (meV)	Method	Ref.
7783.4(22)	$\geq 3/2^+$	1.8(7)	(p, γ)	[Ste96]
7801(2)	$5/2^+$ (IAS)	2.2(10)	$\beta p, \beta \gamma$	Present
7854.8(15)	$7/2^+, 9/2^{+\,b}$	15.8(34)	(p, γ)	[Ste96]
8016(6)	$3/2^{+\,b}$	68(20)	(p, γ)	[Seu90]
8058(7)		37(12)	(p, γ)	[Seu90]
8164.1(12)	$5/2^{+\,a}$	235(33) [c]	(p, γ)	[Ste96]
8288(3)		364(60)	(p, γ)	[Seu90]
8334(8)		95(30)	(p, γ)	[Seu90]

[a] From [End90].

[b] From [Sch95b].

[c] From [Seu90].

Our reaction rate prediction based on [Ste96 and Publication 3] for ^{22}Na$(p,\gamma)^{23}$Mg at 10^8 K is about three times more precise than the prediction given by [Sch95b]. This can be seen in Fig. 3.3, where both of these predictions are plotted as functions of the temperature. The result achieved improves the precision of understanding the operation of NeNa cycle at the important temperature region around 10^8 K.

The proton-capture lifetime $\tau_p(^{22}$Na$)$ is related to the reaction rate as [Seu90]

$$\tau_p = \frac{1}{\rho X_H N_A \langle \sigma v \rangle} \qquad (3.2.5)$$

where ρ is the density and X_H the mass fraction of hydrogen. The density ρ has to be given in units of mole m^{-3}. By comparing τ_p with τ_β we can get information on feeding to the p and β^+ channels in chosen stellar conditions.
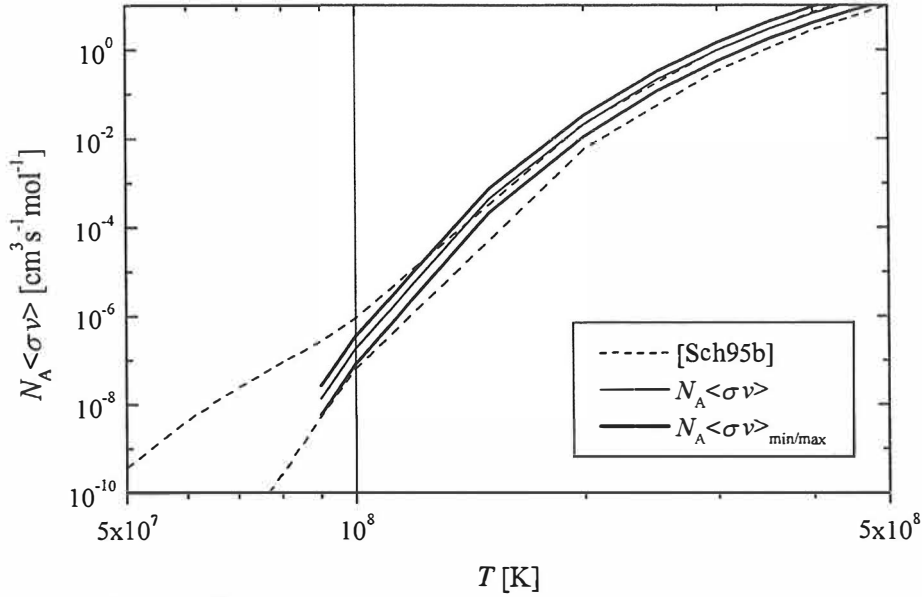

Fig. 3.3. ^{22}Na(p,γ)^{23}Mg reaction rate as a function of the temperature. The thin solid line corresponds to the calculated reaction rate and the thick solid lines define its uncertainty.

At temperatures of 3×10^8 K and above, the NeNa cycle disappears and a continuous reaction flow towards heavier nuclides starts to develop [Wie86]. This reaction flow is called the rp process.

3.3. Beta decay of ^{58}Cu

Spin-isospin excitations are important in probing nuclear structure at low and high excitation energies. Among these, the Gamow–Teller (GT) transitions provide an important tool to study such excitations for all nuclei, especially those far from the valley of beta stability. Nuclear beta decay provides a direct method to obtaining GT strength and its distribution, but with the well-known limitation set by the decay Q value. To overcome this problem, Goodman et al. [Goo80] proposed in 1980 that for the (p, n)

30

charge-exchange reaction the cross section at $0°$ scattering angle, i.e. $\sigma(0°)$, is expected to be proportional to the GT transition strength, $B(GT)$, at projectile energies of about 120 MeV. This proportionality was soon afterwards extended to charge-exchange reactions done with heavier projectiles, such as (^{3}He, t) [Ber87] and (^{6}Li, ^{6}He) [Wir90]. Equation (3.3.1) below shows more precisely how $\sigma(0°)$ and $B(GT)$ are assumed to be connected [Ber87]. This is the low-momentum-transfer approximation to the differential cross section in the distorted-wave Born approximation. Expression (3.3.1) includes also a possible Fermi part:

$$\frac{d\sigma(0°)}{d\Omega} = \left(\frac{\mu}{\pi\hbar^2}\right)^2 \frac{k_f}{k_i}\left[N_{\sigma\tau}|J_{\sigma\tau}|^2\langle M_{GT}\rangle^2 + N_\tau|J_\tau|^2\langle M_F\rangle^2\right] \qquad (3.3.1)$$

Here μ is the reduced relativistic mass, $k_{i,f}$ are the initial and final wave numbers, $N_{\sigma\tau,\tau}$ are the distortion factors and $J_{\sigma\tau,\tau}$ are the effective interaction strengths. Testing this relationship between $\sigma(0°)$ and $B(GT)$ is of the utmost importance in using charge-exchange reactions as a probe of GT excitations.

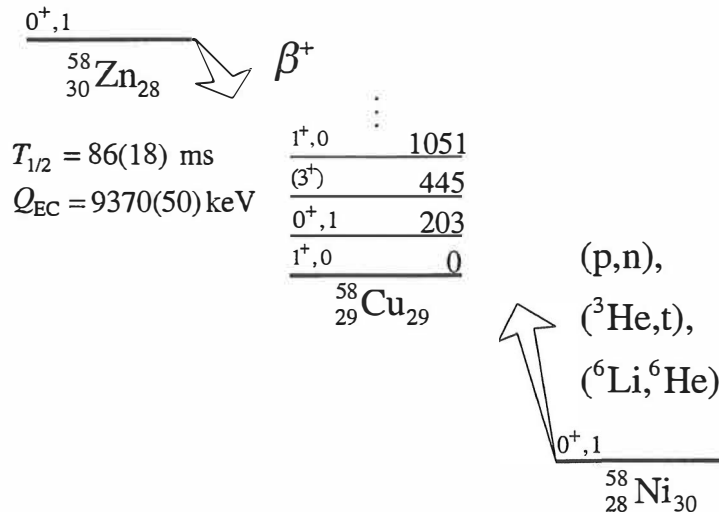Two experiments have recently been carried out to study GT excitations in ^{58}Cu (see Fig. 3.4).

Fig. 3.4. Two different approaches to study GT excitations in ^{58}Cu.

Firstly, a high-resolution charge-exchange reaction experiment employing the ^{58}Ni(^{3}He, t)^{58}Cu reaction was employed to investigate the isospin dependence of GT excitations [Fuj96]. Secondly, a pilot experiment on the beta decay of ^{58}Zn was performed at ISOLDE to extract the beta strength distribution [Jok98]. The beta-decay experiment on ^{58}Zn provides a comparison between the B(GT) values and the charge-exchange cross sections over a broad energy interval [Q_{EC} = 9370(50) keV]. In these studies the ground-state-to-ground-state GT strength from ^{58}Cu beta decay of Jongsma et al. [Jon72] was used to provide the normalization factor between $\sigma(0°)$ and the corresponding B(GT) value. In practice, the GT strength extracted from the work of Jongsma et al. has to be modified before it is suitable for the normalization. Namely, the change of J_i from 1 (^{58}Cu$_{g.s.}$) to 0 (^{58}Ni$_{g.s.}$) induces a change in $\langle M_{GT} \rangle^2$ [see Eq. (3.1.6)]. The main results of these studies are collected in Table 3.2. Also a result from a pioneering (p, n) work is included [Rap82, Rap 83].

Table 3.2. Gamow–Teller strengths to low-lying states in ^{58}Cu. For charge-exchange reactions B(GT; g.s.) is derived from the work of Jongsma et al. [Jon72].

Source	B(GT; g.s.)	B(GT; 1051)	Ref.
(p, n)	0.264(6)	0.72(14)	[Rap82, Rap83]
(^{3}He, t)	0.264(6)	0.46(10)	[Fuj96]
^{58}Zn(β^+)	≤0.31	0.54(26)	[Jok98]

The ^{58}Cu beta-decay experiment described in [Jon72] gives a value of 82(2)% for the ground-state beta branch. However, since that experiment was done without mass separation and [Jon72] did not include sufficient experimental details on the annihilation geometry, there was a need to remeasure this quantity and aim for better accuracy. For this reason, and in view of the importance of this quantity as discussed above, the ground-state branching in ^{58}Cu was indeed recently remeasured independently at GSI and Jyväskylä. At GSI the total absorption spectroscopy was applied [Jan99] while at Jyväskylä the ground-state branch was determined by measuring the total beta-decay intensity which goes via excited states to the ground-state of ^{58}Ni.

The measurement made at Jyväskylä, using the IGISOL facility, is reported in Publication 4 of this thesis. In that work the [58]Cu activity was produced via the [58]Ni(p,n) reaction using 18 MeV beam energy. Mass-separated [58]Cu ions were implanted into a transport tape and moved to the annihilation location (see Fig. 3.5). Data were collected simultaneously at the annihilation and implantation locations. Data from the annihilation location were used to determine the ground-state branch in the beta decay of [58]Cu. Data from the implantation location were used for monitoring and identifying transitions. As our main calibration activity we used the well-known beta decay of [54m]Co [Fir96].
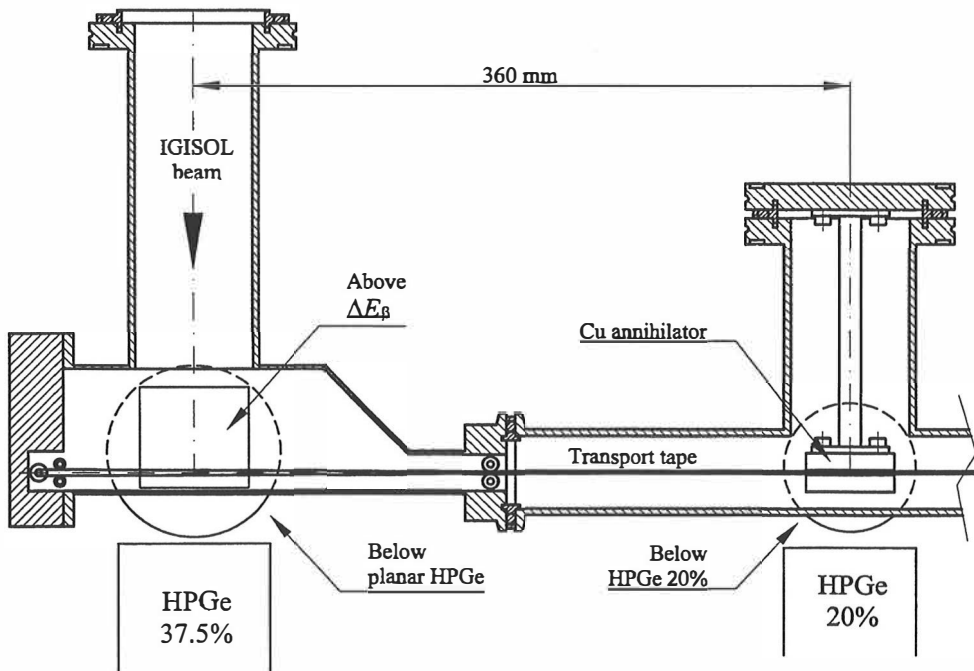

Fig. 3.5. Measurement setup used in the [58]Cu experiment.

As the result of this remeasurement we obtained 80.8(7)% for the ground-state beta decay branch. This value is in agreement with [Jon72] but three times more precise. The remeasurement performed at GSI gave 81.2(5)% [Jan99]. By taking the weighted average of these values we get 81.1(4)% for the ground-state branch. The measured ground-state branchings together with the well-known half-life of 3.204(7) s and $Q_{EC} = 8563.0(21)$

keV allow us to calculate the corresponding $\log ft$ and $\langle M_{GT} \rangle^2$ values for each of the three measurements. By taking the weighted average of the extracted $\log ft$ and $\langle M_{GT} \rangle^2$ values we get $\log ft = 4.873(2)$ and $\langle M_{GT} \rangle^2 = 0.0514(3)$. This $\langle M_{GT} \rangle^2$ is four times more accurate than that of [Jon72] and can be used to improve GT studies. Especially the present knowledge of the beta decay of ^{58}Zn can be improved by utilizing new developments related to the production of pure Zn beams at ISOLDE and efficient detection of beta-delayed proton decays.

4. Summary and Outlook

The first part of this thesis work is devoted to the development of a fluid-dynamical model. Such updating was timely due to increased computing power. The purpose was to learn more about the relation between thermal motion and macroscopic flow from the single-ion point of view. The idea was to develop a model which is accurate but at the same time as simple as possible. As a first step we developed a method to compute the macroscopic flow field inside a stopping chamber. The validity of the boundary conditions was tested with measurements. In the next step, thermal motion and macroscopic flow were combined into a unified model. This model was tested by measurements on laser resonance ionization and evacuation time. The simulated and measured results were in good agreement.

Efficiency and delay-time measurements, made by studying ^{219}Rn recoils from the alpha decay of ^{223}Ra, showed that ^{219}Rn recoils may come out from the gas-catcher/ion guide gas cell in a multiple charge state. Ions up to charge state +4 were observed. Also +1 ion survival times (half-life) in plasma-free conditions were estimated. All these studies were made with He as the buffer gas.

The beta decay of ^{23}Al to excited states in ^{23}Mg was studied as a first nuclear spectroscopy application. For the first time, a $T = 3/2$ isobaric analogue state (IAS), at 7801(2) keV, was observed to decay by both proton and gamma emission. This observation is also important for astrophysics because the proton and gamma widths of this state make important contributions to the hot NeNa cycle. Also three other beta-delayed gamma rays from ^{23}Al were observed for the first time in this work.

The ground-state beta decay branch of ^{58}Cu was remeasured as a second nuclear spectroscopy application. The motivation for this remeasurement was to produce a more precise calibration standard for ^{58}Ni(^{3}He, t)^{58}Cu charge-exchange reaction studies. This charge-exchange reaction gives GT strengths over a wider energy range than does ^{58}Zn beta decay. In this approach the GT strength from the ground-state-to-ground-state beta

decay of ^{58}Cu is needed to provide the normalization factor between the cross section near 0° scattering angle and the corresponding B(GT).

References

[AEA94]   AEA Technology Computational Fluid Dynamics Services, CFDS-FLOW3D User Guide (Oxfordshire, 1994).

[And90]   J. D. Anderson Jr., Modern compressible flow: with historical perspective (McGraw-Hill, New York, 1990).

[Atk90]   P. W. Atkins, Physical Chemistry (Freeman, New York, 1990).

[Aud95]   G. Audi, A. H. Wapstra, Nucl. Phys. A 595 (1995) 409.

[Bér94]   R. Béraud, A. Emsallem, A. Astier, R. Bouvier, R. Duffait, Y. Le Coz, S. Morier, A. Wojtasiewicz, Yu. A. Lazarev, I. V. Shirokovsky, I. N. Izosimov, D. Barnéoud, J. Genevey, A. Gizon, R. Guglielmini, G. Margotton, J. L. Vieux-Rochaz, Nucl. Instr. and Meth. in Phys. Res. A 346 (1994) 196.

[Ber87]   I. Bergqvist, A. Brockstedt, L. Carlén, L. P. Ekström, B. Jakobsson, C. Ellegaard, C. Gaarde, J. S. Larsen, C. Goodman, M. Bedjidian, D. Contardo, J. Y. Grossiord, A. Guichard, R. Haroutunian, J. R. Pizzi, D. Bachelier, J. L. Boyard, T. Hennino, J. C. Jourdain, M. Roy-Stephan, M. Boivin, P. Radvanyi, Nucl. Phys. A 469 (1987) 648.

[Bru77]   P. J. Brussaard, P. W. M. Glaudemans, Shell Model Applications in Nuclear Spectroscopy (North-Holland, New York, 1977).

[Cha92]   A. E. Champagne, M. Wiescher, Annu. Rev. Nucl. Part. Sci. 42 (1992) 39.

[Den97]   P. Dendooven, Nucl. Instr. and Meth. in Phys. Res. B 126 (1997) 182.

[Den98a]   P. Dendooven, S. Hankonen, A. Honkanen, M. Huhta, J. Huikari, A. Jokinen, V. S. Kolhinen, G. Lhersonneau, A. Nieminen, M. Oinonen, H. Penttilä, K. Peräjärvi, J. C. Wang, J. Äystö, Nuclear Fission and Fission-Product Spectroscopy: Second International Workshop, edited by G. Fioni et al. (The American Institute of Physics, 1998) p. 135.

[Den98b]   P. Dendooven, R. Béraud, E. Chabanat, A. Emsallem, A. Honkanen, M. Huhta, A. Jokinen, G. Lhersonneau, M. Oinonen, H. Penttilä, K. Peräjärvi, J. C. Wang, J. Äystö, Nucl. Instr. and Meth. in Phys. Res. A 408 (1998) 530.

[Des87]   Ph. Dessagne, Ch. Miehé, Strasbourg, CRN report CRN PN 87-08, unpublished.

[End90]   P. M. Endt, Nucl. Phys. A 521 (1990) 1.

[Ewa80]   G. T. Ewan, E. Hagberg, J. C. Hardy, B. Jonson, S. Mattsson, P. Tidemand-Petersson, I. S. Towner, Nucl. Phys. A 343 (1980) 109.

[Fir96]   R. B. Firestone, V. S. Shirley, Table of isotopes, 8th ed. (Wiley, New York, 1996).

[Flu98]   Fluent Incorporated, User's guide (Lebanon, 1998).

[Fon86]   A. Fontell, J. Maula, R. Nieminen, C. Söderlund, K. Valli, A. Vehanen, M. Vulli, M. Ylilammi, Tyhjiötekniikka (INSKO ry:n kirjapaino, 1986).

[Fuj96]   Y. Fujita, A. Akimune, I. Daito, M. Fujiwara, M. N. Harakeh, T. Inomata, J. Jänecke, K. Katori, H. Nakada, S. Nakayama, A. Tamii, M. Tanaka, H. Toyokawa, M. Yosoi, Phys. Lett. B 365 (1996) 29.

38

[Goo80]   C. D. Goodman, C. A. Goulding, M. B. Greenfield, J. Rapaport, D. E. Bainum, C. C. Foster, W. G. Love, F. Petrovich, Phys. Rev. Lett. 44 (1980) 1755.

[Gou72]   R. A. Gough, R. G. Sextro, J. Cerny, Phys. Rev. Lett. 28 (1972) 510.

[Gov71]   N. B. Gove, M. J. Martin, Nucl. Data Tables 10 (1971).

[Hon97]   A. Honkanen, P. Dendooven, M. Huhta, G. Lhersonneau, P. O. Lipas, M. Oinonen, J.-M. Parmonen, H. Penttilä, K. Peräjärvi, T. Siiskonen, J. Äystö, Nucl. Phys. A 621 (1997) 689.

[Jan99]   Z. Janas, M. Karny, Y. Fujita, L. Batist, D. Cano-Ott, R. Collatz, P. Dendooven, A. Gadea, M. Gierlik, M. Hellström, Z. Hu, A. Jokinen, R. Kirchner, O. Klepper, F. Moroz, M. Oinonen, H. Penttilä, A. Plochocki, E. Roeckl, B. Rubio, M. Shibata, J. L. Tain, V. Wittman, GSI Annual Report (1999) 13.

[Jok98]   A. Jokinen, M. Oinonen, J. Äystö, P. Baumann, P. Dendooven, F. Didierjean, V. Fedoseyev, A. Huck, Y. Jading, A. Knipper, M. Koizumi, U. Köster, J. Lettry, P. O. Lipas, W. Liu, V. Mishin, M. Ramdhane, H. Ravn, E. Roeckl, V. Sebastian, G. Walter, the ISOLDE Collaboration, Eur. Phys. J. A 3 (1998) 271.

[Jon72]   H. W. Jongsma, A. G. Da Silva, J. Bron, H. Verheul, Nucl. Phys. A 179 (1972) 554.

[Jos99]   J. José, A. Coc, M. Hernanz, Astrophys. J. 520 (1999) 347.

[Kan95]   J. Kantele, Handbook of Nuclear Spectrometry (Academic Press, London, 1995).

[Kud96]   Y. Kudryavtsev, J. Andrzejewski, N. Bijnens, S. Franchoo, J. Gentens, M. Huyse, A. Piechaczek, J. Szerypo, I. Reusen, P. Van Duppen, P. Van Den Bergh, L. Vermeeren, J. Wauters, A. Wöhr, Nucl. Instr. and Meth. in Phys. Res. B 114 (1996) 350.

[PCO98]   PCO Computer Optics, Operating Instructions SensiCam (Kelheim, 1998).

[Pen97]   H. Penttilä, P. Dendooven, A. Honkanen, M. Huhta, P. P. Jauho, A. Jokinen, G. Lhersonneau, M. Oinonen, J.-M. Parmonen, K. Peräjärvi, J. Äystö, Nucl. Instr. and Meth. in Phys. Res. B 126 (1997) 213.

[Qam94]   Z. N. Qamhieh, Ph.D. Thesis, Catholic University of Leuven, 1994.

[Rap82]   J. Rapaport, T. Taddeucci, T. P. Welch, D. J. Horen, J. B. McGrory, C. Gaarde, J. Larsen, E. Sugarbaker, P. Koncz, C. C. Foster, C. D. Goodman, C. A. Goulding, T. Masterson, Phys. Lett. B 119 (1982) 61.

[Rap83]   J. Rapaport, T. Taddeucci, T. P. Welch, C. Gaarde, J. Larsen, D. J. Horen, E. Sugarbaker, P. Koncz, C. C. Foster, C. D. Goodman, C. A. Goulding, T. Masterson, Nucl. Phys. A 410 (1983) 371.

[Ras96]   M. Rasi, R. Saintola, K. Valli, Nucl. Instr. and Meth. in Phys. Res. A 378 (1996) 251.

[Rav94]   H. L. Ravn, P. Bricault, G. Ciavola, P. Drumm, B. Fogelberg, E. Hagebø, M. Huyse, R. Kirchner, M. Mittig, A. Mueller, H. Nifenecker, E. Roeckel, Nucl. Instr. and Meth. in Phys. Res. B 88 (1994) 441.

[RIA00]   http://www.nscl.msu.edu/research/ria /home.html.

[Sch95a]   K. Schreckenbach, P. Liaud, R. Kossakowski, H. Nastoll, A. Bussiere, J. P. Guillaud, Phys. Lett. B 349 (1995) 427.

[Sch95b]   S. Schmidt, C. Rolfs, W. H. Schulte, H. P. Trautvetter, R. W. Kavanagh, C. Hategan, S. Faber, B. D. Valnion, G. Graw, Nucl. Phys. A 591 (1995) 227.

[Seu90]   S. Seuthe, C. Rolfs, U. Schröder, W. H. Schulte, E. Somorjai, H. P. Trautvetter, F. B. Waanders, R. W. Kavanagh, H. Ravn, M. Arnould, G. Paulus, Nucl. Phys. A 514 (1990) 471.

[Ste96]   F. Stegmüller, C. Rolfs, S. Schmidt, W. H. Schulte, H. P. Trautvetter, R. W. Kavanagh, Nucl. Phys. A 601 (1996) 168.

[Tan97]   J. C. Tannehill, D. A. Anderson, R. H. Pletcher, Computational fluid dynamics and heat transfer (Taylor and Francis, Washington, 1997).

[Tas89]   P. Taskinen, H. Penttilä, J. Äystö, P. Dendooven, P. Jauho, A. Jokinen, M. Yoshii, Nucl. Instr. and Meth. in Phys. Res. A 281 (1989) 539.

[Tig95]   R. J. Tighe, J. C. Batchelder, D. M. Moltz, T. J. Ognibene, M. W. Rowe, J. Cerny, B. A. Brown, Phys. Rev. C 52 (1995) R2298.

[Tow95]   I. Towner, E. Hagberg, J. C. Hardy, V. T. Koslowsky, G. Savard, Int. conf. on exotic nuclei and atomic masses, ENAM 95, Arles, 1995, eds. M. De Saint Simon and O. Sorlin (Editions Frontiers, Gif-Sur-Yvette, 1995) p. 711.

[Vie95]   L. A. Viehland, E. A. Mason, Atom. Data Nucl. Data Tables 60 (1995) 37.

[Wie86]   M. Wiescher, K. Langanke, Z. Phys. A 325 (1986) 309.

[Wir90]   H. Wirth, E. Aschenauer, W. Eyrich, A. Lehmann, M. Moosburger, H. Schlösser, H. J. Gils, H. Rebel, S. Zagromski, Phys. Rev. C 41 (1990) 2698.

[Ärj81a]   J. Ärje, K. Valli, Nucl. Instr. and Meth. 179 (1981) 533.

[Ärj81b]   J. Ärje, J. Äystö, J. Honkanen, K. Valli, A. Hautojärvi, Nucl. Instr. and Meth. 186 (1981) 149.

[Ärj86]   J. Ärje, Ph.D. thesis, University of Jyväskylä, 1986.

[Äys77]   J. Äystö, Ph.D. thesis, University of Jyväskylä, 1977.

[Äys01]   J. Äystö, Nucl. Phys. A, to be published.